



Cite this: *RSC Adv.*, 2020, **10**, 20358

A highly hydrophilic benzenesulfonic-grafted graphene oxide-based hybrid membrane for ethanol dehydration†

Lin Tang, Yingying Lu, Lulu Yao * and Peng Cui*

A new type of hybrid membrane was prepared by blending sodium alginate (SA) with benzenesulfonic-grafted graphene oxide (BS@GO), which showed higher hydrophilicity and more defects or edges than GO to create channels for the transfer of water molecules. BS@GO was synthesized by reacting aryl diazonium salts with graphene oxide (GO). The BS@GO sheets were aligned parallelly to the membrane surface and affected the interactions between the SA chains. BS@GO could improve the hydrophilicity and pervaporation properties of SA-based hybrid membranes. Also, compared to GO fillers, BS@GO fillers could supply higher water permeance to improve the pervaporation flux and separation factor. For the pervaporation of 90 wt% aqueous ethanol at 343 K, the optimum hybrid membrane with 1.5 wt% BS@GO in the SA matrix showed the maximum permeate flux of $703 \pm 89 \text{ g m}^{-2} \text{ h}^{-1}$ (1.4 times higher than that of an SA membrane), and the highest separation factor was 5480 ± 94 (5.6 times higher than that of the SA membrane). Moreover, the hybrid membrane exhibited good stability and separation ability during long-term testing.

Received 23rd March 2020
 Accepted 29th April 2020

DOI: 10.1039/d0ra02668a
rsc.li/rsc-advances

1. Introduction

Pervaporation is a progressive and high-efficiency separation technology for the dehydration of organic aqueous solutions to replace some traditional separation methods (such as distillation, azeotropic distillation, and adsorption) due to its simple operation, low energy consumption, high sustainability and high selectivity.^{1–3} Effective separation membranes should possess good selectivity, permeability and stability.^{4–6} Currently, pervaporation membranes mainly include organic membranes, inorganic membranes and organic–inorganic hybrid membranes. The organic membranes usually consist of polymer materials with excellent treating ability; however, they suffer from easy swelling and mediocre selectivity. Inorganic membranes (zeolite, silica, ceramic, *etc.*) have good chemical stability and excellent separation performance; however, they are brittle and expensive and show poor workability. Reddy *et al.* revealed different nano-fillers used in the functionalization of various polymer matrices with enhanced properties.^{7–14} Inorganic fillers such as carbon nanotubes (CNTs),^{15,16} graphene oxide (GO),¹⁷ cerium oxide (CeO₂),¹⁸ zirconium oxide (ZrO₂),¹⁹ titanium dioxide (TiO₂),²⁰ graphitic carbon nitride (g-C₃N₄)^{21,22}

and metal–organic frameworks (MOFs)²³ have been introduced into polymer matrices to form hybrid membranes in order to overcome the intrinsic limitations of organic or inorganic polymers as membrane materials.

Graphene oxide (GO) has atomic thickness, high specific surface area and extraordinary physical properties. The unique structure of GO, which is composed of hydrophilic regions (including hydroxyl, carboxyl and epoxy groups) and hydrophobic regions (aromatic rings), can realize the rapid transmission of water molecules; therefore, it has attracted wide attention.^{24–26} Self-assembly is an effective and popular method to prepare GO-based membranes. The membranes composed of GO sheets showed high flux for ethanol dehydration by pervaporation.²⁷ Membranes were fabricated through the layer-by-layer self-assembly of gelatin and GO and utilized for ethanol dehydration by pervaporation.²⁸ The double-crosslinking strategy was used to adjust the interlayer spacing of GO-based pervaporation membranes to improve their performance in isopropanol dehydration.²⁹

However, self-assembled GO membranes reveal poor stability in high-concentration aqueous solutions. Organic–inorganic hybrid membranes show excellent stability and pervaporation properties for dehydration. Cha-Umpong *et al.* fabricated GO-based composite membranes to desalinate concentrated inland brine by pervaporation and investigated the transport of water molecules and hydrated cations through them.^{30,31} Cao *et al.* prepared reduced GO (rGO) to blend with a sodium alginate (SA) matrix. The rGO-based SA hybrid membrane showed increased separation factors and unusual

School of Chemistry and Chemical Engineering, Hefei University of Technology, Anhui Province Key Laboratory of Controllable Chemistry Reaction and Material Chemical Engineering, Hefei 230009, China. E-mail: yaolulu166@hfut.edu.cn; cuipeng@hfut.edu.cn

† Electronic supplementary information (ESI) available. See DOI: [10.1039/d0ra02668a](https://doi.org/10.1039/d0ra02668a)



changes in its permeation fluxes.³² Both cation-functionalized GO (lignin-decorated GO) and zwitterionic GO (PSBMA@GO)-based SA matrix hybrid membranes expressed much more promising pervaporation performance compared with bare SA polymer membrane.^{20,33} Carboxyl graphene (CG) obtained by the carboxylation reaction of GO was incorporated in the PVA matrix *via* high-power ultrasonic treatment and showed high separation performance for ethanol/water and methanol/MTBE mixtures.³⁴

Benzenesulfonic group-modified GO with large electronegativity showed stronger hydrophilic and ethanol repellence than pristine GO (provided only by -COOH, -OH and epoxy groups).^{33,35} The benzenesulfonic groups on the modified GO surface could bind abundant water molecules to form a hydration layer, which preferentially accelerated the transport of water molecules and repelled ethanol molecules in the feed solution.³³ At the same time, the interlayer spacing of the inner GO sheets increased along with the connection of $-\text{SO}_3\text{H}$ groups and large-volume benzene rings. The stability and dispersibility were enhanced for the same reasons.³⁶ Furthermore, the establishment of covalent bonds between the benzenesulfonic groups and grafted GO could produce more defects and edges on the GO sheets, which endowed the channels with high selectivity and fast transport for water molecules.²¹ Therefore, the hybrid membranes prepared by blending benzenesulfonic-grafted GO with hydrophilic polymers show potential to improve the performance of pervaporation separation.

In this paper, benzenesulfonic-grafted GO (BS@GO) was prepared by modifying GO with 4-aminobenzenesulfonic acid. The physicochemical structure and hydrophilicity of BS@GO sheets and SA-BS@GO hybrid membranes were characterized. The performance of the hybrid membranes in pervaporation dehydration was evaluated with ethanol aqueous solutions. The influences of the BS@GO content, operating temperature and feed solution concentration on the separation performance were studied. The mechanism of SA-BS@GO hybrid membranes for improving pervaporation performance was discussed as well.

2. Experimental

2.1 Materials

Graphene oxide (GO, membrane diameter 0.5–5 m) was purchased from XFNANO Ltd (Nanjing, China). Sodium alginate (SA, CP), 4-aminobenzenesulfonic acid (AR), hydrochloric acid (GR), and absolute ethanol (AR) were purchased from Shanghai Aladdin Biochemical Technology Co., Ltd (Shanghai, China). Anhydrous calcium chloride (AR), sodium nitrite (AR) and sodium hydroxide (AR) were supplied by Sinopharm Chemical Reagent Co., Ltd (Shanghai, China). Nylon microfiltration membranes (pore size 0.2 μm) were purchased from Tianjin Jinteng Experiment Equipment Co., Ltd (Tianjin, China).

2.2 Synthesis of BS@GO

BS@GO was synthesized by reaction of a synthetic aryl diazonium salt with graphene oxide, as shown in Fig. S1.^{†37} First, 4-

aminobenzenesulfonic acid (1 g), HCl solution (12 mL, volume of ice water : concentrated HCl = 5 : 1) and NaNO₂ (0.4 g) were sequentially added to NaOH (20 mL, 2.0 wt%) solution with stirring. The reaction was maintained at 273 K for 15 min to form an aryl diazonium salt. The product was then added to a GO suspension (200 mL, 1 mg mL⁻¹) and stirred for 4 h in an ice bath, then washed with water and centrifuged until the pH of the solution was near neutral. The freeze-drying process afforded BS@GO.

2.3 Fabrication of hybrid membranes

A nylon filter with an average pore diameter of 0.2 μm was used as a substrate of the composite membrane. A BS@GO aqueous dispersion was prepared and dispersed by sonication for 1 h. Then, magnetic stirring was carried out at 303 K for 4 h to obtain a uniform SA-BS@GO casting solution. The concentration of SA in the obtained casting solution was 1.5 wt% and the concentration of BS@GO in SA was 0 wt%, 1.0 wt%, 1.5 wt%, 2.0 wt%, or 3.5 wt%. The casting solutions were placed at room temperature for 1 h to remove bubbles from the solution. The cast membrane droplets were coated on a porous nylon membrane substrate and dried at room temperature. The dried membranes were immersed in CaCl₂ solution (0.5 M) for 10 min, rinsed several times with deionized water, and then dried at room temperature again. The resulting membranes were named SA-BS@GO-X (X represents the mass ratio of BS@GO to SA). The corresponding homogeneous membranes for the characterization tests were prepared on glass plates instead of nylon filters by a similar preparation procedure.

2.4 Measurement of separation performance

The permeation separation performance of the composite membranes was evaluated by a pervaporation separation technique using water/ethanol mixtures. The pervaporation experiments were carried out on a self-made device in the laboratory. Under the action of the vacuum pump, the absolute pressure on the downstream side of the membrane was controlled under 0.4 kPa. The effective area of the membrane was 9.62 cm², and the flow rate of the feed liquid was controlled at 25 L h⁻¹. The membrane reached a steady state, and the permeate was collected in a cold trap immersed in liquid nitrogen. The permeate was weighed and the composition was measured by gas chromatography. The main pervaporation data of permeation flux (J , g m⁻² h⁻¹) and the separation factor (α) were calculated separately as follows:³⁸

$$J = \frac{Q}{A \times t} \quad (1)$$

$$\alpha = \frac{P_{\text{W}}/P_{\text{E}}}{F_{\text{W}}/F_{\text{E}}} \quad (2)$$

In eqn (1) and (2), Q (g) is the mass of the permeate (g), t is the time interval (h), and P and F are the mass ratios of water (subscript W) and ethanol (subscript E) of the feed and permeate, respectively.



2.5 Calculation of activation energies by the Arrhenius equation

The relationship between the operating temperature and permeate flux was determined by the Arrhenius equation.³⁹

$$J_i = J_0 e^{-E_a/RT} \quad (3)$$

In eqn (3), J_i ($\text{g m}^{-2} \text{ h}^{-1}$) is the rate constant, J_0 ($\text{g m}^{-2} \text{ h}^{-1}$) is the pre-factor (also called the frequency factor), E_a (kJ mol^{-1}) is the apparent activation energy, R ($\text{kJ mol}^{-1} \text{ K}^{-1}$) is the molar gas constant and T (K) is the thermodynamic temperature. Take $R = 8.314 \times 10^{-3} \text{ kJ mol}^{-1} \text{ K}^{-1}$, and take the logarithm of the equation as in eqn (4):

$$\ln J_i = \ln A - \frac{E_a}{8.314} \times \frac{1000}{K} \quad (4)$$

Therefore, by plotting the line graph of $\ln J_i$ vs. $1000/T$, the value of E_a can be obtained.

2.6 Driving force normalized form of permeation flux and selectivity calculation

In order to prove the intrinsic properties of the hybrid membrane, the permeability was further calculated by the equation $(P/I)_i$ (gas permeation unit (GPU), 1 GPU = $7.501 \times 10^{-12} \text{ m}^3$ (STP) $\text{m}^{-2} \text{ s}^{-1} \text{ Pa}^{-1}$) and the selectivity (β) as follows:^{40,41}

$$(P/I)_i = \frac{J_i}{\gamma_{io} \chi_{io} P_{io}^{\text{sat}} - P_{il}} \quad (5)$$

$$\beta = \frac{(P/I)_w}{(P/I)_e} \quad (6)$$

In eqn (5) and (6), J_i ($\text{g m}^{-2} \text{ h}^{-1}$) is the flux of substance I and γ_{io} , χ_{io} and P_{io}^{sat} are the activity coefficients, mole fraction and saturated vapor pressure of component i in the feed, respectively. P_{io} and P_{il} (Pa) are the partial pressure of the feed side and the permeate side of component i , respectively; they can be considered to be zero under high vacuum conditions. γ_{io} and P_{io}^{sat} were calculated by Aspen simulation and the Antoine equation, respectively.

2.7 Characterization

The roughness data of the membrane surfaces were obtained by atomic force microscopy (AFM, Dimension, Germany) in the X - Y direction; the typical scanning range was $90 \mu\text{m} \times 90 \mu\text{m}$, and the height distribution range of the GO or BS@GO sheets was $10 \mu\text{m} \times 10 \mu\text{m}$. X-ray photoelectron spectroscopy (XPS, ESCALAB 250Xi, Japan) was used to analyse the elements contained in the samples. The zeta potentials of the samples were measured by a Zetasizer Nano (Nano-ZS90, England). The morphologies of the membranes were observed by a field emission scanning electron microscope (FESEM, SU8020, Japan). X-ray diffraction (XRD, X'Pert PRO MPD, Netherlands) with a scan range between 5° and 60° and a scan speed of 5° min^{-1} at room temperature was used to study the chemical compositions of GO and BS@GO to determine the crystal structure of the successfully grafted and mixed

membrane of 4-aminobenzenesulfonic acid. Raman spectroscopy (Raman, LabRAM HR Evolution) was carried out with an incident laser with a 514 nm wavelength. The chemical structures of GO, BS@GO and the membranes were analysed by Fourier transform infrared spectroscopy (FT-IR, Nicolet 67, America) with a scan range of 4000 – 500 cm^{-1} . Thermal performance was obtained in a temperature range of 298 – 873 K (heating rate 10 K min^{-1}) using thermogravimetric analysis (TGA, STA 449F5, Germany) and differential scanning calorimetry (DSC, DSC 214, Germany) with a temperature range of 303 – 473 K . The hydrophilicity of the membranes was measured by a static contact angle meter with about $5 \mu\text{L}$ pure water drop (CA, Jinzhitang, China). The pervaporation unit tested the separation properties and the effects of the operating conditions.

3. Results and discussion

3.1 Characterization of BS@GO

The FT-IR spectra of GO and BS@GO are shown in Fig. 1a. The stretching vibration peaks of the C–H bonds in the benzene ring, hydroxyl group ($-\text{OH}$), carboxyl group ($-\text{COOH}$), and carboxylate salt ($-\text{COO}^-$) are located at 2919 cm^{-1} , 2853 cm^{-1} , 3364 cm^{-1} , 1727 cm^{-1} and 1616 cm^{-1} , respectively.^{42,43} For BS@GO, two new peaks appeared at 1219 cm^{-1} and 1064 cm^{-1} , which are related to the stretching vibrations of $\text{S}=\text{O}$ and $\text{S}–\text{O}$ bonds, respectively; this indicates the successful introduction of benzenesulfonic groups. The addition of benzenesulfonic groups increased the disorder of carbon in the graphite plane (Fig. 1b), and BS@GO exhibited a higher I_D/I_G value (1.03) than GO (0.94); this indicates that more sp^3 hybridized carbon and more structural defects appeared on BS@GO than on GO.^{44,45} The elemental composition was further investigated by X-ray photoelectron spectroscopy (XPS), as shown in Fig. 1c and S2,† S element was introduced into the GO by benzenesulfonic group functionalization. In Fig. 1c, the peaks of $\text{S} 2s$ and $\text{S} 2p$ appear in the spectrum of BS@GO. For the $\text{S} 2p$ spectral fitting peaks, denoted in Fig. S2,† a main peak at around 168 eV corresponds to sulfonate functional groups, indicating that S was in the form of sulfonic acid.⁴⁶ These results

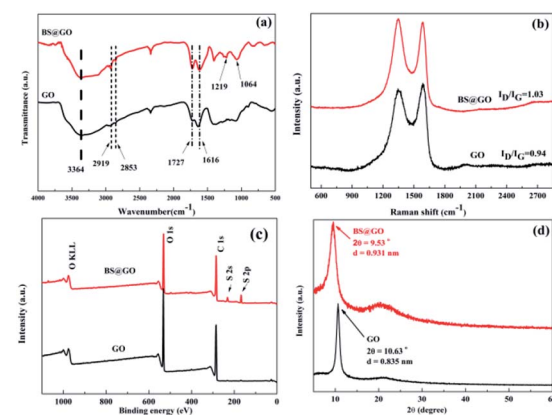


Fig. 1 (a) FT-IR spectra of GO and BS@GO; (b) Raman spectra of GO and BS@GO; (c) XPS surveys of GO and BS@GO; and (d) XRD patterns of GO and BS@GO.



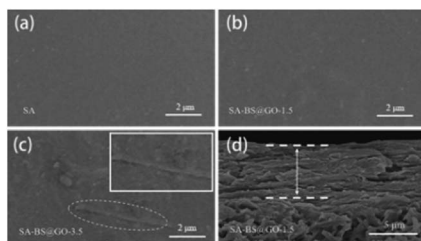


Fig. 2 Surface morphologies of (a) SA; (b) SA-BS@GO-1.5; (c) SA-BS@GO-3.5 and (d) cross-section morphology of the SA-BS@GO-1.5 membrane.

indicate that BS@GO contained benzenesulfonic groups. This result could be confirmed by the XRD spectra (Fig. 1d). Because of the relatively large molecular size of the benzenesulfonic groups between the sheets, the interlayer spacing of BS@GO calculated using the Debye–Scherrer equation was 0.931 nm, which was larger than that of GO (0.835 nm).

BS@GO showed a higher zeta potential absolute value than GO, as shown in Fig. S3; † thus, BS@GO can be stable in aqueous solution. Therefore, BS@GO showed excellent water dispersion compared to GO, as shown in Fig. S4.† Just as GO had been successfully modified by benzenesulfonic groups, BS@GO showed poorer affinity to ethanol.^{32,47} The BS@GO precipitated easily while GO tended to remain suspended in ethanol, as shown in Fig. S4.†

3.2 Physicochemical properties of the SA-BS@GO-X membranes

The morphologies of the hybrid membranes SA-BS@GO-1.5 and SA-BS@GO-3.5 were compared with that of SA membrane. From the surface morphology pictures in Fig. 2(a–c), all the membranes were smooth and dense. However, the SA-BS@GO-3.5 membrane showed wrinkles due to its plentiful BS@GO sheets.²⁵ The cross-sectional morphology of SA-BS@GO-1.5 revealed that a dense layer about 5 µm thick was tightly supported by the honeycomb nylon substrate (Fig. 2d). The porous honeycomb nylon substrate endowed the hybrid membranes with sufficient mechanical strength and negligible permeate resistance. The dense layer should act as the active layer during the pervaporation progress. AFM images in the 4 × 4 µm² scanning area (Fig. S5†) confirmed the SEM results, with inconspicuous differences in both the surface roughness and morphology between the SA and SA-BS@GO-1.5 membranes. As shown in the XRD patterns in Fig. S6,† neither new bonds of BS@GO nor bond shifts appeared

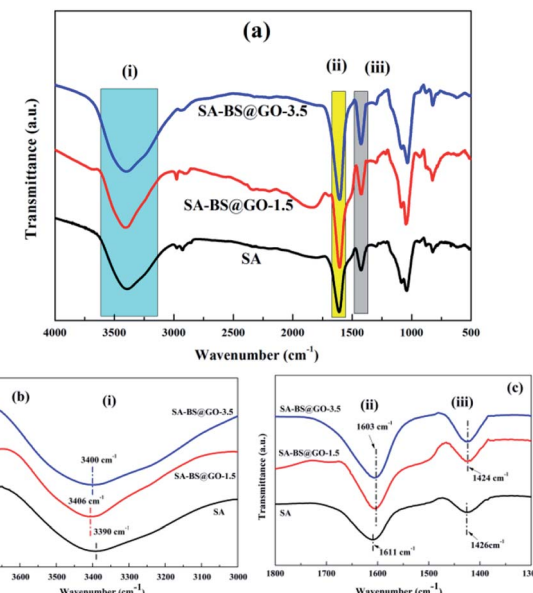


Fig. 4 FT-IR spectra of the SA and SA-BS@GO-X hybrid membranes: (a) whole spectra; (b) spectra of region (i); (c) spectra of regions (ii) and (iii).

with the different dosages of BS@GO in SA; it can be ascertained that the BS@GO sheets were distributed homogeneously inside the SA matrix, which is identical to results in published papers.^{25,32}

The cross-sectional images captured from the active layer showed differences in the membranes of SA and SA-BS@GO-X, as shown in Fig. 3. The cross-section of SA was relatively smooth and homogeneous, as shown in Fig. 3a. Fig. 3b and c denote that the BS@GO sheets tended to arrange horizontally in the membrane surface of the SA matrix.²⁵ In the SA-BS@GO-1.5 matrix, the filler sheets were arranged in an orderly manner parallel to the membrane surface (the yellow dashed lines mark the parallel direction of the BS@GO sheets in Fig. 3b). Fig. 3c revealed that the filler sheets may suffer from overlapping and curving (called agglomeration) at the SA-BS@GO-3.5 matrix. When agglomeration occurs, the advantages of the filler sheets cannot be fully exploited.²⁵

The chemical structures of the pure SA and SA-BS@GO-X hybrid membranes were studied by FT-IR, as shown in Fig. 4. For all of the membranes, similar characteristic peaks of the stretching vibration of the –OH group (i region), symmetric stretching vibration of the –COO[–] group (ii region), and asymmetric stretching vibration of the –COO[–] group (iii region)

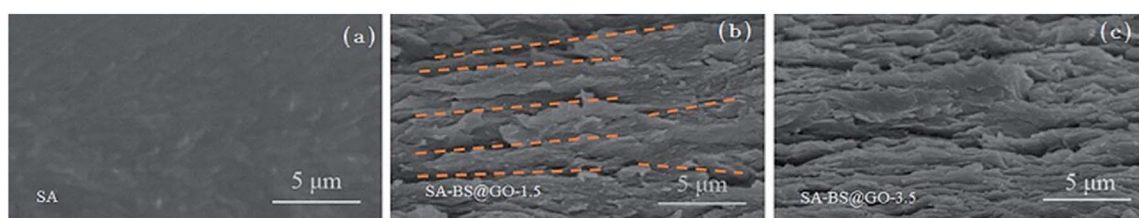


Fig. 3 Cross-section images of the matrices of (a) SA; (b) SA-BS@GO-1.5; (c) SA-BS@GO-3.5.

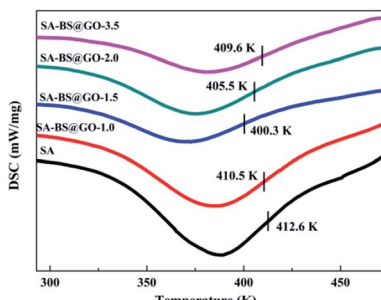


Fig. 5 DSC curves of the SA and SA-BS@GO-X hybrid membranes.

could be designated at $\sim 3400\text{ cm}^{-1}$, $\sim 1610\text{ cm}^{-1}$, and $\sim 1425\text{ cm}^{-1}$, respectively (Fig. 4a). The peaks at 1100 cm^{-1} and 822 cm^{-1} can be attributed to C–O–C of aliphatic ether and cyclic ether from the SA matrix and were identical among the different membranes. Meanwhile, in region (i), the band shifted from 3390 cm^{-1} (pure SA membrane) to 3406 cm^{-1} (SA-BS@GO-1.5 membrane) and then to 3400 cm^{-1} (SA-BS@GO-3.5 membrane). Also, in regions (ii) and (iii), red shifts were observed from 1611 cm^{-1} and 1426 cm^{-1} (pure SA membrane) to 1603 cm^{-1} and 1424 cm^{-1} (SA-BS@GO-1.5 and SA-BS@GO-3.5 membranes), respectively. It can be deduced that H-bonds were formed between the $-\text{COO}^-$ groups of SA and the $-\text{phSO}_3\text{H}$ groups of the BS@GO sheets in the hybrid membranes, as shown in Fig. S7.† The H-bonds between the hydroxyl groups inside the SA matrix were weakened, and the weakened effect was decreased by the agglomeration of excessive BS@GO sheets. These results were reinforced by the T_g and DSC data (Fig. 5).

As shown in Fig. 5, as the H-bonds weakened with increasing dosage from 0 to 1.0 wt% and 1.5 wt% inside the SA matrix, the glass transition temperature (T_g) of the hybrid polymers decreased from 412.6 K to 410.5 K and 400.3 K, then enhanced again to 405.5 K and 409.6 K when the mass contents of BS@GO were 2.0 wt% and 3.5 wt%, respectively. The stronger the H-bonds between SA chains, the higher the T_g revealed by the membrane. Therefore, the filler of BS@GO sheets could mobilize the SA matrix at no more than 1.5 wt% in the hybrid membranes. However, large amounts of filler (more than 1.5 wt%) agglomerated to obstruct the chain mobility.⁴⁸

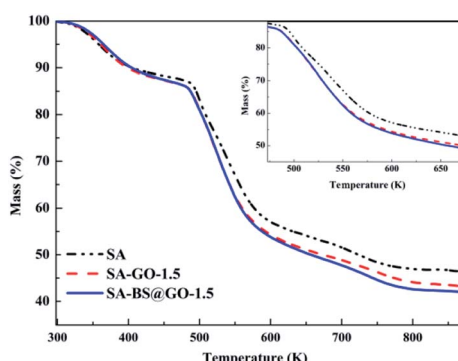


Fig. 6 TGA curves of the different membrane samples.

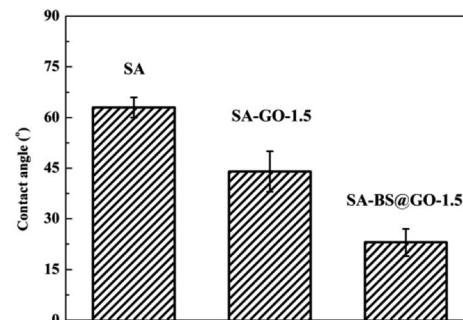


Fig. 7 Contact angles of the SA, SA-GO-1.5 and SA-BS@GO-1.5 membranes.

3.3 Comparing the SA-based hybrid membranes with GO fillers

As reported in the literature, GO can improve the pervaporation properties of SA-based hybrid membranes by improving not only the permeation fluxes but also the separation factors.^{32,49} A control membrane with a GO doping amount of 1.5 wt% was accordingly fabricated for comparison and labelled SA-GO-1.5.

The thermal stabilities of the SA, SA-GO-1.5 and SA-BS@GO-1.5 hybrid membranes were evaluated by TGA under a nitrogen atmosphere. The TGA results are shown in Fig. 6. The DTG results are shown in Fig. S8,† and the parameters are shown in Table S1.† From the thermogravimetric results, the decomposition process of the hybrid membrane involves three stages.^{48,50,51} The first stage (under 473 K) is the evaporation of trace water within the polymer. The functional groups on the SA chains with the oxygen-containing functional groups in GO or BS@GO (e.g. $-\text{SO}_3\text{H}$, $-\text{OH}$, $-\text{COOH}$ and epoxy groups) mainly decomposed in the second stage (473–673 K). The third stage from 673 K to 873 K was due to the pyrolysis of the SA polymer backbone. The different hybrid membranes exhibited nearly the same thermal stability and thermal decomposition behaviour as the SA membrane. This testing temperature was much higher than the actual separation operating temperature ($\leq 343\text{ K}$), ensuring sufficient thermal stability of the membranes. The weight loss rate increased in the order of SA, SA-GO-1.5, SA-GO@BS-1.5 in the second stage of 473–673 K, which can be explained by the maximum functional groups on GO@BS and the minimum functional groups in pure SA. SA and the added sheets are both hydrophilic substances. The contact angle order of SA-BS@GO-1.5 < SA-GO-1.5 < SA can be seen in Fig. 7. Therefore, it can be confirmed that BS@GO filler can improve the hydrophilic properties of SA-based membranes more than GO.

SA and the added sheets are both hydrophilic substances. The contact angle order of SA-BS@GO-1.5 < SA-GO-1.5 < SA can be seen in Fig. 7. Therefore, it can be confirmed that BS@GO filler can improve the hydrophilic properties of SA-based membranes more than GO.

The pervaporation properties (90 wt% ethanol/water mixed solution feed, 323 K) of the SA, SA-GO-1.5 and SA-BS@GO-1.5 membranes are shown in Fig. 8. Both the flux and separation



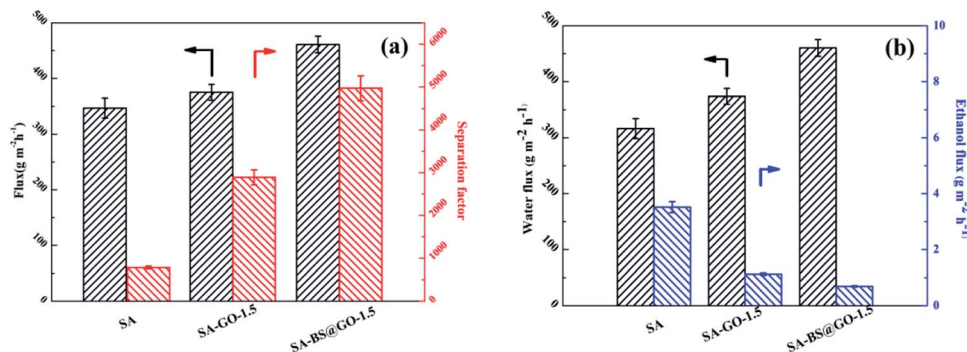


Fig. 8 Pervaporation properties of the SA, SA-GO-1.5 and SA-BS@GO-1.5 membranes: (a) total flux and separation factor; (b) water flux and ethanol flux.

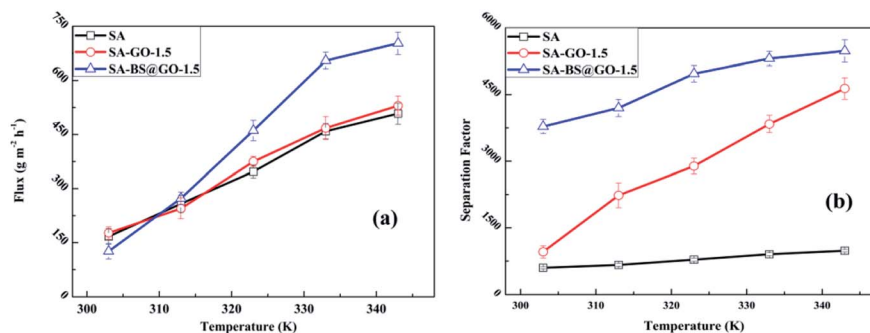


Fig. 9 Pervaporation results at different operation temperatures: (a) flux and (b) separation factor.

were promoted in the order of SA, SA-GO-1.5, SA-BS@GO-1.5 (Fig. 8a). In the literature, GO plays a similar role to BS@GO in SA-based hybrid membranes during dehydration by pervaporation with its transport pathways consisting of hydrophobic aromatic rings and hydrophilic oxygenated groups.^{25,32,49} Benefiting from the high hydrophilicity and ethanol repellence endowed by the benzenesulfonic groups of BS@GO, the water flux increased and the ethanol flux decreased more obviously than with GO (Fig. 8b).

In Fig. 9, the SA, SA-GO-1.5 and SA-BS@GO-1.5 membranes show gradually increasing fluxes and separation factors as the temperature increases from 303 K to 343 K. As the pervaporation of the three membranes was operated in the same conditions of temperature and feed content, the pervaporation characteristics can be explained by the permeance (GPU) and selectivity (Fig. S9†) as well as by the normalized driving force and membrane thickness calculated by eqn (5) and (6).

In the range of 303–343 K, the water permeance value of the SA-BS@GO-1.5 membrane was obviously larger than that of the SA-GO-1.5 membrane, while the water permeance value of the SA-GO-1.5 membrane was slightly larger than that of the SA membrane. On the other hand, the ethanol permeance value of the SA membrane was significantly higher than that of the SA-GO-1.5 membrane, while the SA-BS@GO-1.5 membrane showed a lower value than the SA-GO-1.5 membrane in the operation temperature range. Therefore, it was determined that the GO filler hindered permeation of ethanol, while the benzenesulfonic structures on BS@GO accelerated the water

transmittance. Thus, the flux of the SA-GO-1.5 membrane was slightly higher than that of the SA membrane and remarkably smaller than that of the SA-BS@GO-1.5 membrane, especially at higher temperature. The separation factor of the SA-GO-1.5 membrane was larger than that of the SA membrane, and this gap gradually enlarged as the temperature rose. At the same time, the SA-BS@GO-1.5 membrane showed the highest separation factor in the operation temperature range.

3.4 Properties of the SA-BS@GO-X membranes

The effects of the BS@GO content in the hybrid membranes were determined by studying their hydrophilicity and pervaporation.

Fig. 10 shows that the hydrophilic BS@GO fillers could decrease the contact angle of the SA-BS@GO-X hybrid matrix when the content was no more than 1.5 wt%; however, excessive

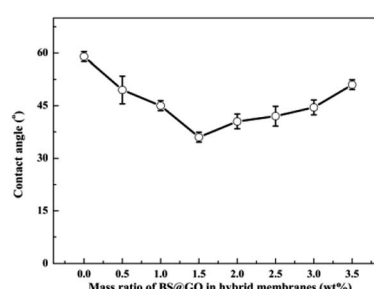


Fig. 10 Contact angles of the SA-BS@GO-X membranes with different mass ratios.

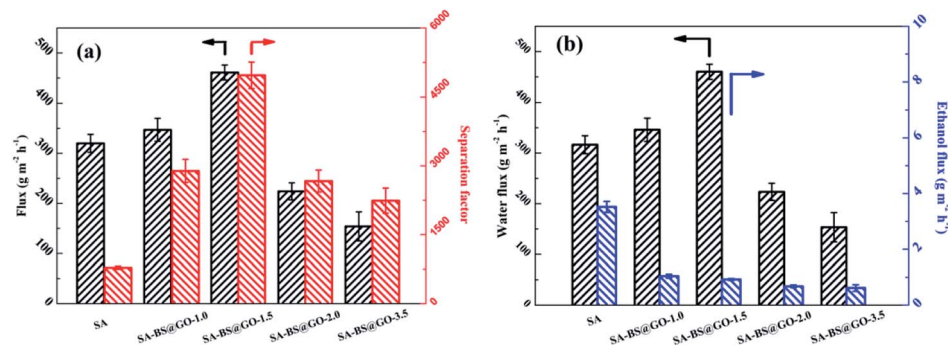


Fig. 11 Pervaporation results of the SA-BS@GO-X membranes: (a) total flux and separation factor; (b) water flux and ethanol flux.

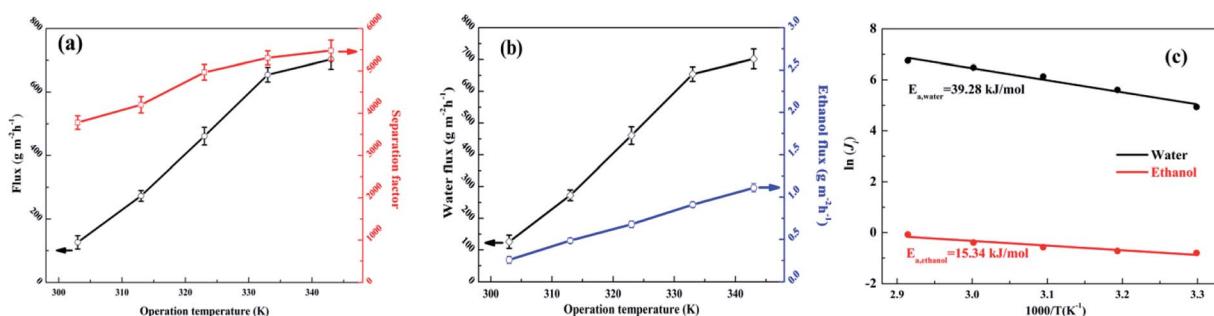


Fig. 12 Effects of operation temperature on the pervaporation performance of the SA-BS@GO-1.5 membrane: (a) total flux and separation factor; (b) water flux and ethanol flux; (c) Arrhenius plots for the permeation flux.

(more than 1.5 wt%) fillers had the opposite effect. Therefore, appropriate hydrophilic BS@GO fillers can enhance the water affinity of the hybrid membranes, but agglomeration may be counterproductive. The addition of BS@GO was beneficial to the enrichment of water molecules on the surface of the separation membrane.⁵²

The dehydration results by pervaporation of the SA-BS@GO-X membranes are displayed in Fig. 11. The pervaporation was performed with 90 wt% ethanol/water mixed solution feed at 323 K. The sample SA-BS@GO-1.5 with moderate BS@GO doping content showed the highest factor and flux. The ethanol flux decreased monotonically from 3.5 g m⁻² h⁻¹ to 0.6 g m⁻² h⁻¹ as the BS@GO doping increased from 0 to 3.5 wt%. This was due to the synergy of ethanol repellence (Fig. S4[†]) and the hindering effect of BS@GO. The water flux increased from 316.5 g m⁻² h⁻¹ to 460.1 g m⁻² h⁻¹ due to the improved hydrophilicity of the BS@GO filler and promoted the mobility of the SA matrix (from the T_g results, Fig. 5). More BS@GO could decrease the water flux to 153 g m⁻² h⁻¹ (SA-BS@GO-3.5). Therefore, the separation factor increased from 781 (SA) to 4969 (SA-BS@GO-1.5) sharply, then decreased to 2240 (SA-BS@GO-3.5).

3.5 Effects of the operation conditions on the pervaporation performance

The optimized membrane of SA-BS@GO-1.5 was used to study the effects of the operation conditions on the pervaporation performance.

The effects of the operation temperature (303–343 K) were investigated with a feed of 90 wt% ethanol/water mixed solution and are shown in Fig. 12(a and b). The water flux, ethanol flux, total flux and separation factor increased with increasing temperature. The increments of the fluxes with higher operation temperature were attributed to the improved driving force (higher partial pressure on the upstream side while the downstream side remains under vacuum), accelerated polymer chain mobility and enhanced thermodynamic movement of the permeate molecules.^{32,50,53} As shown in Fig. S9,[†] for the SA-BS@GO-1.5 membrane, the ethanol permeance showed low absolute values and decreased obviously with increasing temperature, while the water permeance fluctuated in a relatively small range with very high absolute values. This suggests that the driving force is the dominant parameter for the permeation flux.²⁵ Meanwhile, the membranes showed slight swelling in 90 wt% ethanol–water, as in the literature; therefore, membrane swelling was not the primary cause of the permeance.²⁵ The selectivity (β) showed a rapidly rising trend with increasing temperature, which indicates that the ethanol molecules encountered higher transport resistance under high temperature.²⁵

The apparent activation energy (E_a) is described by the Arrhenius equation in eqn (3). The E_a value of water (39.28 kJ mol⁻¹) was larger than that of ethanol (15.34 kJ mol⁻¹), as shown in Fig. 12c. The positive E_a value indicates that the transmembrane process was endothermic, and the permeation processes of both water and ethanol were dominated by diffusion.⁴⁸ It can be seen



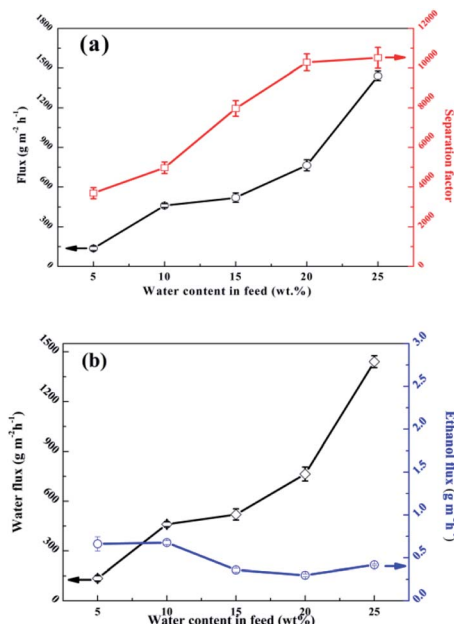


Fig. 13 Effects of the feed composition on the pervaporation performance of the SA-BS@GO-1.5 membrane: (a) total flux and separation factor; (b) water flux and ethanol flux.

that water was more sensitive towards temperature variation. Therefore, it can be ascertained that a higher temperature resulted in a higher separation factor.³²

Fig. 13 shows the effects of the feed composition at 323 K on the separation performance. The study found that the total flux (Fig. 13a) and water flux (Fig. 13b) increased while the ethanol flux (Fig. 13b) decreased in the water concentration range from 5 wt% to 25 wt%. An obvious increase in the water concentration in the feed caused increasing water pressure; therefore, the driving force of the water increased and the driving force of the ethanol receded. Moreover, a higher water concentration in the feed liquid can cause slight swelling of the polymer membrane, which facilitates the penetration of both the water and ethanol molecules.⁵⁴ The separation factor should be elevated significantly with the combined effect of a remarkable increase in water flux and a slight decrease in ethanol flux due to partial pressure and membrane expansion.

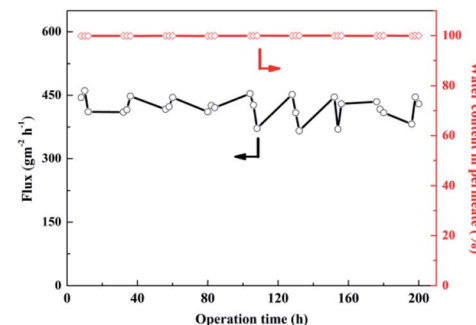


Fig. 15 Long-term operation evaluation of the SA-BS@GO-1.5 membrane.

3.6 Transport mechanism in the hybrid membrane

The transport mechanism in the hybrid membranes is proposed and schematically diagrammed in Fig. 14. The BS@GO sheets with moderate contents were aligned parallel to the membrane surface in the SA matrix. The BS@GO sheets showed excellent hydrophilicity, benefitting from the benzenesulfonic groups. Furthermore, the BS@GO fillers could weaken the H-bonds between the SA chains to diminish the water molecule transport resistance in the SA matrix. During the pervaporation process: (1) the hydrophilic membrane should absorb more water molecules than ethanol molecules; (2) water molecules should be transported through the SA matrix and the low-friction "highways" in the hydrophobic regions of the BS@GO sheet edges and defects, as in GO filler-based membranes;^{32,49} (3) the diffusion of ethanol with a larger kinetic diameter should be restricted by the basal plane (graphene-like area).

3.7 Long-term operation stability

Long-term operation of the SA-BS@GO-1.5 membrane was performed to observe its stability. The SA-BS@GO-1.5 membrane was operated continuously for 200 hours in the pervaporation dehydration process using a 90 wt% ethanol/water feed solution at 323 K. As Fig. 15 shows, because the hybrid membrane had excellent mechanical and thermal properties, the permeate flux of the polymer membrane floated slightly but finally stabilized at about 430 g m⁻² h⁻¹, and the water content in the permeate was generally greater than 99.7 wt%. As shown in Fig. 15, the hybrid membrane was expected to be used in practical applications.

3.8 Comparison of the pervaporation performance of recently reported membranes

The separation performance of the polymer membrane in this study was compared with that of recently reported separation membranes, as shown in Fig. 16 and Table S2 (detailed experimental data†), including SA-based, GO-based, and PVA-based membranes. It can be seen that the hybrid membranes prepared in this work exhibit higher permeation fluxes and separation factors due to the construction of fast transport channels of solvent molecules in the SA matrix and the preference for water molecules. For the membrane in this study, the flux was higher than those of about half of the reported

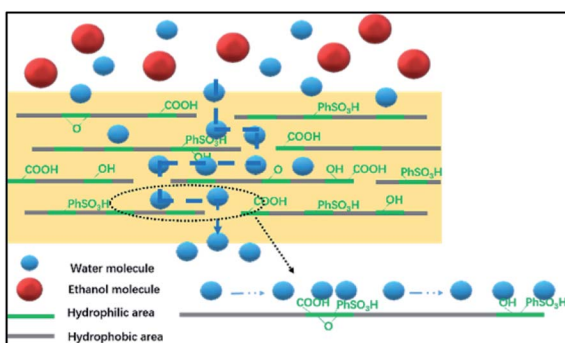


Fig. 14 An illustration of the transport pathways inside the BS@GO membranes.



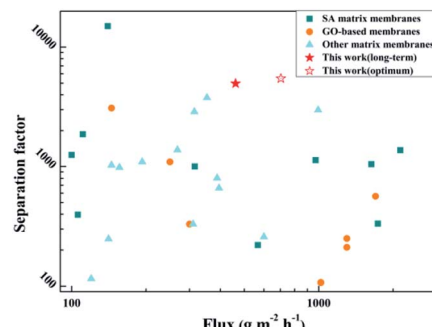


Fig. 16 Comparison of the membrane in this study with recently reported membranes in the literature.

membranes, and the separation factor was higher than those of most of the reported membranes. The SA-BS@GO-1.5 membrane shows excellent comprehensive properties.

4. Conclusions

In this study, GO modified with benzenesulfonic groups (BS@GO) was prepared to construct hybrid membranes with SA to dehydrate ethanol aqueous solutions by pervaporation. The modified BS@GO showed higher hydrophilicity than GO. The SA chains in the hybrid membranes showed higher mobility than those in the SA membrane by the H-bond effect. By means of its ability to block the permeate of ethanol arising from the GO structure and the hydrophilicity originating from benzenesulfonic groups, the hybrid membrane with BS@GO as a filler (SA-BS@GO) showed better properties than the hybrid membrane with GO as a filler (SA-GO) with respect to hydrophilicity, pervaporation fluxes and separation. Overabundant content of BS@GO should be avoided to prevent agglomeration. The optimum BS@GO mass content was 1.5 wt% in the SA matrix. The optimal hybrid membrane, SA-BS@GO-1.5, showed the highest pervaporation flux of $703 \pm 89 \text{ g m}^{-2} \text{ h}^{-1}$ (1.4 times that of the SA membrane) and a separation factor of 5480 (5.6 times that of the SA membrane). The hybrid membrane exhibited excellent long-term separation operation stability. This study provides a versatile and simple method for preparing dense, highly water-selective separation membranes.

Conflicts of interest

There are no conflicts to declare.

Acknowledgements

The authors appreciate the financial support by the National Natural Science Foundation of China (21476055) and the Fundamental Research Funds for the Central Universities (JZ2019HGBZ0169).

References

- 1 M. S. Jyothi, K. R. Reddy, K. Soontarapa, S. Naveen, A. V. Raghu, R. V. Kulkarni, D. P. Suhas, N. P. Shetti, M. N. Nadagouda and T. M. Aminabhavi, *J. Environ. Manage.*, 2019, **242**, 415–429.
- 2 S. Richter, *Environ. Sci. Pollut. Res.*, 2006, **13**, 145.
- 3 D. Hua, R. K. Rai, Y. Zhang and T. S. Chung, *Chem. Eng. Sci.*, 2017, **161**, 341–349.
- 4 R. Castro-Munoz, F. Galiano, V. Fila, E. Drioli and A. Figoli, *Rev. Chem. Eng.*, 2019, **35**, 565–590.
- 5 D. Achari, P. Rachipudi, S. Naik, R. Karuppannan and M. Kariduraganavar, *J. Ind. Eng. Chem.*, 2019, **78**, 383–395.
- 6 P. Liu, M. M. Chen, Y. Q. Ma, C. Hu, Q. G. Zhang, A. M. Zhu and Q. L. Liu, *Chem. Eng. Sci.*, 2019, **206**, 489–498.
- 7 M. Hassan, K. R. Reddy, E. Haque, A. I. Minett and V. G. Gomes, *J. Colloid Interface Sci.*, 2013, **410**, 43–51.
- 8 D. R. Son, A. V. Raghu, K. R. Reddy and H. M. Jeong, *J. Polym. Sci., Part B: Polym. Phys.*, 2016, **55**, 1099–1110.
- 9 K. R. Reddy, K. P. Lee, A. I. Gopalan and H. D. Kang, *React. Funct. Polym.*, 2007, **67**, 943–954.
- 10 S. J. Han, H. I. Lee, H. M. Jeong, B. K. Kim, A. V. Raghu and K. R. Reddy, *J. Polym. Sci., Part B: Polym. Phys.*, 2014, **53**, 1193–1204.
- 11 K. R. Reddy, B. C. Sin, K. S. Ryu, J. Noh and Y. Lee, *Synth. Met.*, 2009, **159**, 1934–1939.
- 12 S. H. Choi, D. H. Kim, A. V. Raghu, K. R. Reddy, H. I. Lee, K. S. Yoon, H. M. Jeong and B. K. Kim, *J. Polym. Sci., Part B: Polym. Phys.*, 2012, **51**, 197–207.
- 13 M. U. Khan, K. R. Reddy, T. Snguanwongchai, E. Haque and V. G. Gomes, *Colloid Polym. Sci.*, 2016, **294**, 1599–1610.
- 14 Y. R. Lee, S. C. Kim, H. I. Lee, H. M. Jeong, A. V. Raghu, K. R. Reddy and B. K. Kim, *Macromol. Res.*, 2011, **19**, 66–71.
- 15 F. B. Peng, C. L. Hu and Z. Y. Jiang, *J. Membr. Sci.*, 2007, **297**, 236–242.
- 16 A. F. Ismail, P. S. Goh, S. M. Sanip and M. Aziz, *Sep. Purif. Technol.*, 2009, **70**, 12–26.
- 17 N. X. Wang, S. L. Ji, G. J. Zhang, J. Li and L. Wang, *Chem. Eng. J.*, 2012, **213**, 318–329.
- 18 T. Tavangar, M. Karimi, M. Rezakazemi, K. R. Reddy and T. M. Aminabhavi, *Chem. Eng. J.*, 2020, **385**, 123787.
- 19 C. V. Reddy, I. N. Reddy, B. Akkinepally, V. V. N. Harish, K. R. Reddy and S. Jaesool, *Ceram. Int.*, 2019, **45**, 15298–15306.
- 20 S. P. Dharupaneedi, S. K. Nataraj, M. Nadagouda, K. R. Reddy, S. S. Shukla and T. M. Aminabhavi, *Sep. Purif. Technol.*, 2019, **210**, 850–866.
- 21 K. T. Cao, Z. Y. Jiang, X. S. Zhang, Y. M. Zhang, J. Zhao, R. S. Xing, S. Yang, C. Y. Gao and F. S. Pan, *J. Membr. Sci.*, 2015, **490**, 72–83.
- 22 K. R. Reddy, C. V. Reddy, M. N. Nadagouda, N. P. Shetti, S. Jaesool and T. M. Aminabhavi, *J. Environ. Manage.*, 2019, **238**, 25–40.
- 23 Q. Q. Li, Q. Liu, J. Zhao, Y. Y. Hua, J. J. Sun, J. G. Duan and W. Q. Jin, *J. Membr. Sci.*, 2017, **544**, 68–78.
- 24 X. K. Cai, T. Luo, B. Liu and H. M. Cheng, *Chem. Soc. Rev.*, 2018, **47**, 6224–6266.
- 25 K. C. Guan, F. Liang, H. P. Zhu, J. Zhao and W. Q. Jin, *ACS Appl. Mater. Interfaces*, 2018, **10**, 13903–13913.
- 26 C. Xue, W. B. Cai, X. H. Chen, Z. Shi and J. D. Li, *RSC Adv.*, 2019, **9**, 15457–15465.



27 T. M. Yeh, Z. Wang, D. Mahajan, B. S. Hsiao and B. Chu, *J. Mater. Chem. A*, 2013, **1**, 12998–13003.

28 J. Zhao, Y. W. Zhu, F. S. Pan, G. W. He, C. H. Fang, K. T. Cao, R. S. Xing and Z. Y. Jiang, *J. Membr. Sci.*, 2015, **487**, 162–172.

29 X. Zhang, M. X. Zhang, H. Ding, H. Yang, X. H. Ma, X. R. Xu, Z. L. Xu and C. Y. Tang, *ACS Omega*, 2019, **4**, 15043–15050.

30 W. Cha-Umpong, G. X. Dong, A. Razmjou and V. Chen, *J. Membr. Sci.*, 2019, **588**, 117210.

31 W. Cha-Umpong, E. Hosseini, A. Razmjou, M. Zakertabrizi, A. H. Korayem and V. Chen, *J. Membr. Sci.*, 2020, **598**, 117687.

32 K. T. Cao, Z. Y. Jiang, J. Zhao, C. H. Zhao, C. Y. Gao, F. S. Pan, B. Y. Wang, X. Z. Cao and J. Yang, *J. Membr. Sci.*, 2014, **469**, 272–283.

33 J. Zhao, Y. W. Zhu, G. W. He, R. S. Xing, F. S. Pan, Z. Y. Jiang, P. Zhang, X. Z. Cao and Y. Wang, *ACS Appl. Mater. Interfaces*, 2016, **8**, 2097–2103.

34 G. L. Han, Z. Chen, L. F. Cai, Y. H. Zhang, J. F. Tian, H. H. Ma and S. M. Fang, *J. Appl. Polym. Sci.*, 2020, **137**, 48526.

35 Y. S. Ye, M. Y. Cheng, X. L. Xie, J. Rick, Y. J. Huang, F. C. Chang and B. J. Hwang, *J. Power Sources*, 2013, **239**, 424–432.

36 J. Wang, M. M. Chen, C. Y. Wang, J. Z. Wang and J. M. Zheng, *J. Power Sources*, 2011, **196**, 550–558.

37 Ravikumar and S. Keith, *Chem. Commun.*, 2012, **48**, 5584–5586.

38 F. B. Peng, L. Y. Lu, C. L. Hu, H. Wu and Z. Y. Jiang, *J. Membr. Sci.*, 2005, **259**, 65–73.

39 K. Huang, G. P. Liu, Y. Y. Lou, Z. Y. Dong, J. Shen and W. Q. Jin, *Angew. Chem. Int. Edit.*, 2014, **53**, 6929–6932.

40 Y. K. Ong, G. M. Shi, N. L. Le, Y. P. Tang, J. Zuo, S. P. Nunes and T. S. Chung, *Prog. Polym. Sci.*, 2016, **57**, 1–31.

41 S. V. Kononova, D. A. Sapegin, E. V. Kruchinina, G. N. Gubanova, K. A. Romashkova, A. L. Didenko, V. E. Smirnova, E. N. Popova, N. N. Saprykina, E. N. Vlasova and V. M. Svetlichnyi, *J. Appl. Polym. Sci.*, 2019, **136**, 48197.

42 Y. Shen and B. L. Chen, *Environ. Sci. Technol.*, 2015, **49**, 7364–7372.

43 J. Gao, F. Liu, Y. L. Liu, N. Ma, Z. Q. Wang and X. Zhang, *Chem. Mater.*, 2010, **22**, 2213–2218.

44 G. X. Zhao, L. Jiang, Y. D. He, J. X. Li, H. L. Dong and X. K. Wang, *Adv. Mater.*, 2011, **23**, 3959–3963.

45 W. Y. Huang, X. L. Ouyang and L. Lee, *J. ACS Nano.*, 2012, **6**, 10178–10185.

46 Y. Xie, M. H. Edward, C. S.-N. Lindsay and A. P. Brian, *Environ. Sci. Technol.*, 2016, **50**, 1821–1827.

47 Z. Q. Jiang, X. S. Zhao and A. Manthiram, *Int. J. Hydrol. Energ.*, 2013, **38**, 5875–5884.

48 B. X. Gao, Z. Y. Jiang, G. H. Liu, R. S. Xing, H. Wu, F. S. Pan, B. Y. Wang and X. Z. Cao, *J. Membr. Sci.*, 2016, **520**, 951–963.

49 J. Zhao, Y. W. Zhu, G. W. He, R. S. Xing, F. S. Pan, Z. Y. Jiang, P. Zhang, X. Z. Cao and B. Y. Wang, *ACS Appl. Mater. Interfaces*, 2016, **8**, 2097–2103.

50 Y. M. Song, Z. Y. Jiang, B. X. Cao, H. J. Wang, M. D. Wang, Z. He, X. Y. Cao and F. S. Pan, *Chem. Eng. Sci.*, 2018, **185**, 231–242.

51 B. Munavalli, A. Torvi and M. Kariduraganavar, *Polymer*, 2018, **142**, 293–309.

52 S. P. Dharupaneedi, R. V. Anjanapura, J. M. Han and T. M. Aminabhavi, *Ind. Eng. Chem. Res.*, 2014, **53**, 14474–14484.

53 M. R. Wang, H. Wu, X. T. Jin, C. Yang, X. Y. He, F. S. Pan, Z. Y. Jiang, C. Y. Wang, M. M. Chen, P. Zhang and X. Z. Cao, *Chem. Eng. Sci.*, 2018, **178**, 273–283.

54 J. Zhao, F. S. Pan, P. Li, C. H. Zhao, Z. Y. Jiang, P. Zhang and X. Z. Cao, *ACS Appl. Mater. Interfaces*, 2013, **5**, 13275–13283.

